

Robust elemental mapping of nanostructures at ultrahigh resolution using event-streamed spectrum imaging in an aberration-corrected analytical electron microscope

A.A. Herzing*, I.M. Anderson

National Institute of Standards and Technology, Material Measurement Laboratory, 100 Bureau Drive, Gaithersburg, MD 20899, USA

ARTICLE INFO

Available online 28 July 2012

Keywords:

XEDS

Spectrum imaging

STEM

Hyperspectral

ABSTRACT

We describe the application of X-ray energy dispersive spectroscopy (XEDS) event-streamed spectral imaging (ESSI) in an aberration-corrected analytical electron microscope (AEM) as a reliable method for the acquisition of ultra-high spatial resolution elemental maps. With the ESSI approach, the XEDS spectral image is acquired over multiple frames at rates typically reserved for imaging experiments. This approach differs significantly from that typically employed in the AEM, where spectrum image data is acquired serially (a pixel at a time) using per-pixel dwell times that are orders of magnitude larger.

The ESSI approach provides numerous advantages, most notably the ability to use the relatively strong transmitted electron image signals as a reference to spatially register the sparse XEDS data. State-of-the-art implementations of ESSI allow this registration to be performed “on-the-fly”, such that drift correction is performed in real time. In addition, the electron dose imparted to the specimen is spread over time, meaning the instantaneous dose at a given point in the specimen is orders of magnitude lower than that imparted using serial spectral imaging. Thus, ESSI enables the high spatial resolution analysis of dose-rate-sensitive specimens. The application of this technique to several nanoscale systems is discussed, along with the potential for its use in combination with improved detector designs.

Published by Elsevier B.V.

1. Introduction

With the development of aberration-correcting electron optics, the acquisition of atomic-resolution images in an analytical electron microscope (AEM) has become commonplace [1] and the ability to perform electron energy-loss spectroscopy (EELS) at similar length scales is being increasingly applied to materials characterization [1–4]. However, the sensitivity of EELS to a number of technologically interesting elements is quite low, rendering some elements inaccessible via this technique. With a varying sensitivity based on fluorescence yield, X-ray energy dispersive spectroscopy (XEDS) is capable of detecting all elements with atomic number greater than that of beryllium ($Z=4$), and thus offers a complementary spectroscopic technique to EELS that can be carried out in the same instrument. In fact, reports of atomic-resolution spectroscopy based on XEDS have recently been published [5,6], and improvements in probe-forming optics and detector design promise to make the technique even more

useful for the characterization of materials at the nano- and atomic-scale.

The reduction in probe-size afforded by correction of the third-order spherical aberration of the objective lens is a major benefit for imaging and microanalysis at high spatial resolution. However, of nearly equal importance is the substantially increased angular-range over which a diffraction-limited probe may be formed once the aberration has been corrected. From the standpoint of performing microanalysis in the AEM, this allows for a significant increase in probe-current with no loss in spatial resolution [7,8]. While this is important for any analytical signal, it is particularly important for XEDS, as the X-ray generation and collection efficiencies in the AEM are extremely low. The former is due to the extremely small interaction volume of the sub-nanometer, high-energy electron probe within a very thin specimen, while the latter is due to the limited collection angle allowed by the restrictive mechanical dimensions of a high-resolution AEM pole-piece, making it difficult to place the commonly-employed lithium-drifted silicon (Si(Li)) detector in close proximity to the specimen. The resulting collection angle of such a detector is generally around 0.1 sr, which represents less than 1% of the total X-ray emission solid angle of 4π sr [9].

* Corresponding author.

E-mail address: andrew.herzing@nist.gov (A.A. Herzing).

Typically, the difficulties related to signal generation and collection in XEDS are compensated by the use of longer per-pixel dwell times. However, simply increasing the probe dwell time also exacerbates the effects of specimen drift, damage, charging, and other instabilities, and these effects become limiting, especially at the very high spatial resolutions achievable in the aberration-corrected AEM. A more effective way to increase the signal above background in an analytical image is to perform multi-frame image integration, and this approach has been used for many years in scanning electron probe techniques [10]. Simply put, it involves the acquisition of several images at very short probe dwell times, which are then averaged in order to produce a less noisy image.

As described previously [11,12], the same multi-frame acquisition approach can be adapted to spatially resolved XEDS elemental analysis via event-streamed spectral imaging (ESSI), and herein we detail the application of this technique as a reliable method for the acquisition of ultra-high spatial resolution elemental maps in an aberration-corrected AEM. With the ESSI approach, the XEDS spectral image is acquired over hundreds or even thousands of frames of the rastered probe at rates typically reserved for imaging experiments (i.e. 1 μ s–100 μ s per pixel). This spectral image paradigm differs markedly from that which is widely available for the AEM, where statistically comparable data sets are acquired serially, a pixel at a time, using orders of magnitude larger per-pixel dwell times, typically 0.1 s–1.0 s. It is important to note that, in an ESSI acquisition, the quoted dwell time is often close to or even less than the pulse-processor shaping time of the XEDS detector (5 μ s–100 μ s for a Si(Li) detector). However, the acquisition system corrects for dead-time, such that the dwell time quoted is, in actuality, a live-time value.

The ESSI approach provides numerous advantages. Most notably, it allows for the relatively strong transmitted electron image signals (i.e. bright-field, high-angle annular dark-field, etc.) to be used as references for spatial registration of the sparse XEDS data. State-of-the-art implementations of ESSI allow this registration to be performed “on-the-fly”, enabling real-time drift correction. In addition, the electron dose imparted to the specimen is spread over time, wherein the instantaneous dose at a given point in the specimen is orders of magnitude lower than that imparted using serial spectral imaging. ESSI can therefore enable the high spatial resolution analysis of dose-rate-sensitive specimens. Finally, whereas in routine use the data acquired over the multiple frames are aligned and integrated to form a compact XEDS spectral image; it is possible to store and process all of the data in its raw form, producing a time-resolved, four-dimensional spectral image, with consequent opportunities for intelligent sampling strategies.

2. Materials and methods

2.1. Sample preparation

2.1.1. PbSe–MoSe₂ misfit-layer compound

Misfit-layer compounds (MLCs) were fabricated using a process described by Heideman et al. [13], whereby alternating layers of various compounds were deposited via chemical vapor-deposition with careful control of the stoichiometric compositions. In the present case, the precursor layers consisted of Pb and Se (atom fraction of Se was 0.5) and Mo and Se (atom fraction of Se was 0.67). Upon annealing, kinetically-driven self-assembly resulted in alternating polycrystalline layers of the two desired constituents: PbSe and MoSe₂. The film was subsequently prepared for AEM analysis by the small-angle cleavage technique [14] followed by thinning to a final thickness of \approx 80 nm in a

focused ion-beam instrument. Among other interesting properties, such structures often exhibit a very low thermal conductivity due to the separation of all layers by a Van der Waals gap that hinders phonon transport.

2.1.2. Pd/C catalyst

A heterogeneous catalyst sample was prepared via incipient wetness impregnation of an activated carbon support by an aqueous solution of PdCl₂, followed by heat treatment at 400 °C in air for 3 h. A specimen was prepared for AEM analysis by dispersing the powder over a holey-carbon film supported by a 300-mesh Cu TEM grid.

2.1.3. Bimetallic catalyst particles for carbon nanotube growth

Carbon nanotubes (CNTs) were grown in-situ in an environmental TEM according to the procedure described in Sharma et al. [15]. Briefly, thin-films of Ni and Au were sequentially deposited via physical vapor deposition of the pristine metals onto a lacey-SiO_x film supported by a Mo TEM grid. The deposited layer thicknesses were such that the resulting specimen contained a nominal loading of 0.2 M fraction of Au. The grid was then inserted into the environmental TEM and heated to 520 °C, causing the metal films to dewet the SiO_x film and form nanoparticles. CNT growth was initiated by exposing the specimen to C₂H₂ (0.4 Pa), and the reaction was terminated after 15 min.

2.2. Analytical electron microscopy

STEM-HAADF imaging and XEDS spectrum imaging were carried out using a Titan 80-300 TEM/STEM¹ operating at an accelerating voltage of 300 kV. The instrument was equipped with a double-hexapole aberration-corrector (CEOS, GmbH) on the probe-forming side of the objective lens, and an EDAX r-TEM system for XEDS analysis. The spectrometer had a nominal collection solid-angle of \approx 0.1 sr and an energy resolution of 143 eV (FWHM Mn-K α).

2.3. XEDS spectrum imaging

For each of the samples, conventional, single-scan spectrum imaging was carried out using the TIA software package (FEI Co.). A STEM-HAADF image of the area of interest was acquired, and sub-regions were then selected by the operator used to acquire the XEDS spectrum image and the drift-correction reference images. The acquisition proceeded serially, on a pixel-by-pixel basis, using a dwell time of 50 ms–1000 ms, with periodic measurements of the spatial drift made by cross-correlation of the current drift-correction region with an image of the same region acquired at the outset of the acquisition.

ESSI was carried out using the same instrument using a 4Pi RevolutionEDX system consisting of an XEDS pulse-processor, a scan generator to drive the electron probe, and a software interface to store the data and to calculate specimen drift. This ESSI system streamed the XEDS and HAADF image signals to the collection PC in a manner that allowed for mapping to be carried out very quickly, with dwell times as low as a few tens of nanoseconds. Typically, drift is corrected during spectrum image acquisition by using the scan coils to physically shift the position of the scan raster. In the case of ESSI, this was accomplished by simply registering the individual frames with each other within

¹ Certain commercial equipment, instruments, or materials are identified in this paper to foster understanding. Such identification does not imply recommendation or endorsement by the National Institute of Standards and Technology, nor does it imply that the materials or equipment identified are necessarily the best available for the purpose.

the confines of the entire dataset. This resulted in a decrease in X-ray counts near the perimeter of the acquisition when significant drift had occurred, since the number of frames that spatially registered with these specimen locations was less than the total number of frames acquired. This was easily compensated by

assuring that the area of interest was not located near the perimeter of the scan raster, or acquiring the data at lower magnification and using higher pixel density to preserve spatial resolution. Since the correction did not involve re-positioning of the electron probe, it could be carried out either in real-time or

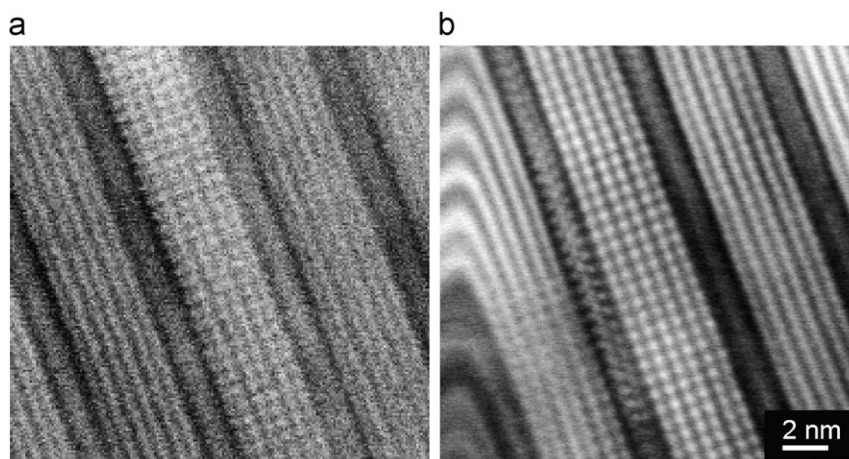


Fig. 1. Results of multi-frame image acquisition of PbSe–MoSe₂ MLC. (a) Single frame acquisition and (b) average image from multi-frame acquisition. Note the presence of a distortion on the left-most portion of (b) due to an insufficient amount of time for flyback correction.

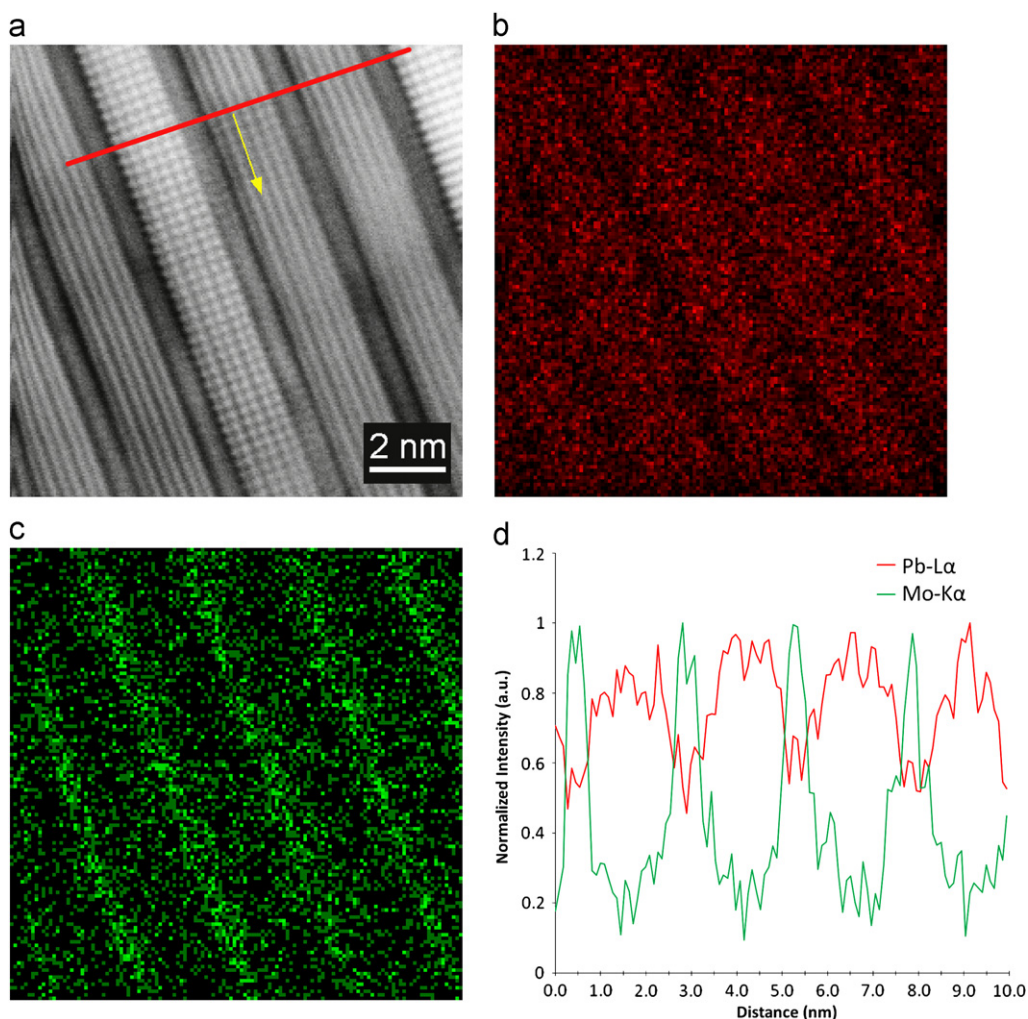


Fig. 2. Results of ESSI acquisition from PbSe–MoSe₂ MLC specimen. (a) Integrated STEM-HAADF intensity from total acquisition, (b) Mo-K α and (c) Pb-L α elemental maps, and (d) line profiles of (b) and (c) extracted along the red-line shown in (a) and integrated along the direction denoted by the yellow line in (a). (For interpretation of the references to color in this figure legend, the reader is referred to the web version of this article.)

after the acquisition. Finally, in order to maximize the speed of the acquisition, at the expense of energy-resolution, short pulse-processor shaping times were normally utilized (i.e. 25 μ s or less).

3. Results and discussion

3.1. Atomic-scale imaging and elemental spectroscopy of engineered nanostructures

As discussed in the Introduction, the basis for the ESSI acquisition is the same as that used for multi-frame image acquisition. The results of such an acquisition are illustrated in Fig. 1, which compares a single, fast-scan image frame with a multi-frame integration image of the alternating PbSe and MoSe₂ MLC. While the single-scan image is adequate for describing the atomic-scale structure present in the larger PbSe layers, the signal above background is not sufficient to conclusively characterize the structure of the single layers of MoSe₂. When integrated over several frames, the true structure of all on-axis regions of the specimen is revealed, with the MoSe₂ adopting the expected dichalcogenide-type structure consisting of a planar array of Mo atoms surrounded on either side by an offset plane of Se atoms. In addition, this system exhibits turbostratic disorder, such that not all layers of the PbSe constituent exhibit the same orientation with respect to the film normal, as evidenced by the lack of on-axis channeling in all but one of the layers. Finally, it should be noted that this particular image was acquired with a very high scan-rate (50 ns per pixel), resulting in a

distortion in the left-most portion of the image. This is the commonly encountered “fly-back” artifact that results when the scan rate significantly exceeds the delay time necessary for relaxation of the inductance imparted to the scan coils in driving the beam to the right side of the image during the previous line of the raster.

ESSI was applied to the same MLC, and the results of this analysis are shown in Fig. 2. In this case, a 256×256 array of pixels was scanned at a rate of 5 μ s per pixel (≈ 0.3 s per frame) using a 0.1 nA probe current. The pixel size was 40.5 pm and 10,000 frames were collected, resulting in a total probe dwell time of 50 ms per pixel. The integrated HAADF image (Fig. 2(a)) shows that the drift-correction was adequate to maintain high-resolution over the course of the acquisition. Elemental maps were extracted for Pb-L α and Mo-K α (despite the higher intensity they exhibited, the Pb-M α and Mo-L α lines were not used due to severe overlap with each other), and these are presented in Fig. 2(b) and (c). The individual maps are quite noisy, reflecting the difficulty in collecting significant signal that was described in the introduction. However, modulation of the intensity is present in each map with increases in signal above background detected in the regions of the specimen where the Pb and Mo signals are expected to be enhanced. This is more conclusively shown in the intensity traces presented in Fig. 2(d), which were generated by extracting the signal along the red line overlaid in Fig. 2(a) and integrating along the in-plane direction, highlighted by the yellow arrow. Here, the Mo signal is strongly peaked over the dichalcogenide columns, while the Pb signal is localized to the bands associated with the rock-salt structure. Interestingly, the intensity

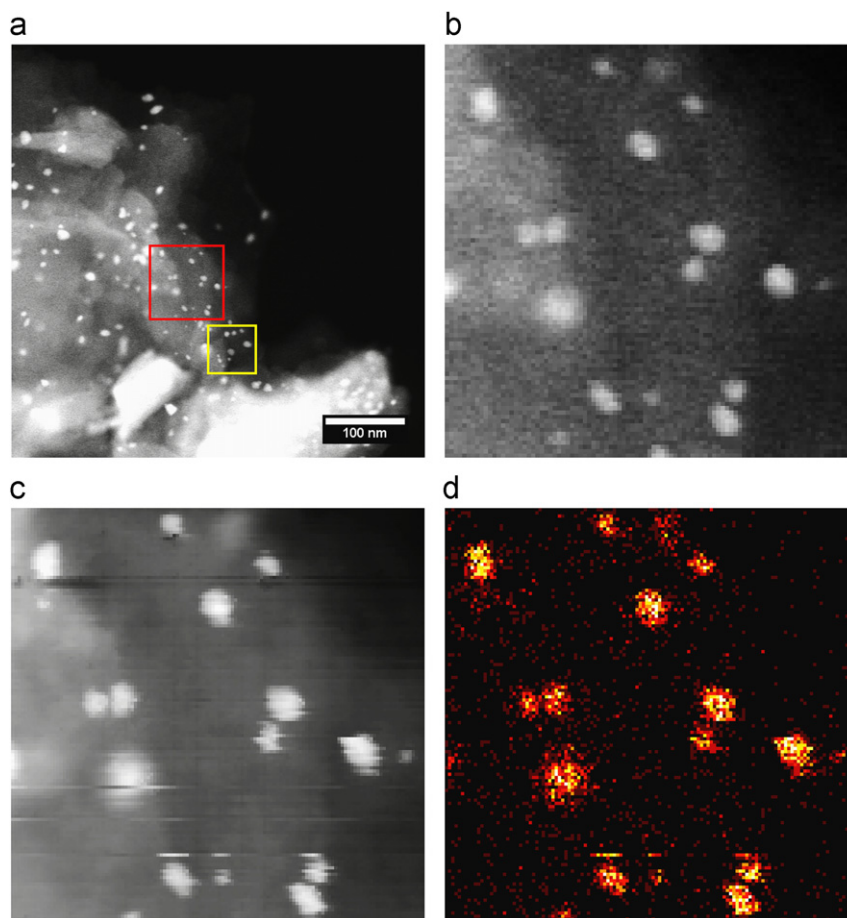


Fig. 3. Results of a single-scan XEDS spectrum image acquisition from a Pd/Carbon heterogeneous catalyst. (a) STEM-HAADF image showing the analytical area (red box) and the area used for the drift-correction analysis (yellow box). (b) Zoomed image of the acquisition area showing the true distribution of particles over the carbon support, (c) real-time HAADF detector output acquired during SI acquisition, and (d) the resulting Pd-L α map. Size of (b)–(d) is 100 nm \times 100 nm. (For interpretation of the references to color in this figure legend, the reader is referred to the web version of this article.)

from the Pb signal never completely decays to zero, even over the MoSe₂ layers. This is likely caused by increased beam broadening [16] within the rock-salt structure due to the much higher atomic mass of the Pb atoms present.

3.2. Comparison of single-scan SI and ESSI for catalyst characterization

To compare the traditional, single-scan SI approach with ESSI, a heterogeneous catalyst sample consisting of Pd particles immobilized on an activated-carbon support was examined. Equivalent

datasets were acquired using the two acquisition schemes such that the spatial resolution and the total dwell time per pixel were the same. In practice, ESSI allows for a larger specimen region to be analyzed at the same spatial-resolution, since spatial drift can be mitigated over the course of the increased acquisition time necessary for such pixel densities.

The pixel dimensions were held constant at ≈ 1 nm and the total dwell time per pixel was 60 ms (note: as discussed in the Introduction, all dwell times given are live-time corrected). Specifically, the single-scan data set, shown in Fig. 3(a), consisted of a 128×128 array of pixels (red box) selected from a previously

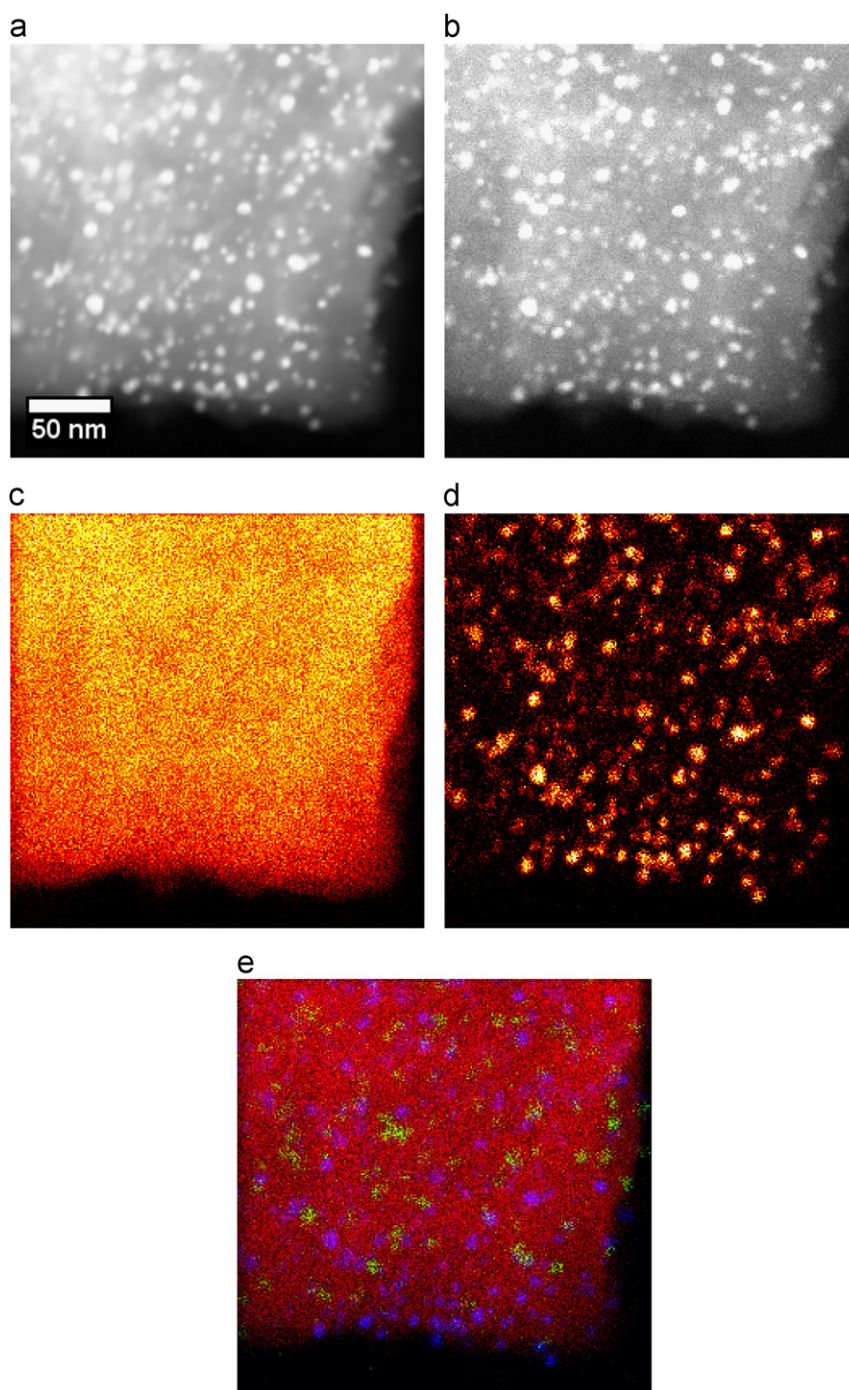


Fig. 4. Results of ESSI acquisition from a Pd/carbon heterogeneous catalyst. (a) STEM-HAADF integrated over the entire acquisition, (b) initial STEM-HAADF image acquired at the outset, resulting (c) C-K α and (d) Pd-L α XEDS maps, and (e) color overlay showing the distributions of carbon (red), palladium (blue), and oxide impurity (green) constituents. Scale bars in all images are the same as in (a). (For interpretation of the references to color in this figure legend, the reader is referred to the web version of this article.)

acquired STEM-HAADF image. Spatial drift was corrected via periodic cross-correlation with a reference image (Fig. 3(a), yellow box) carried out every 64 pixels (or every ≈ 4 s). Fig. 3(b) is a zoomed-in view of the analytical region showing its nominal structure. A quick comparison of the features in this image with those present in the HAADF image collected during the SI acquisition and the resulting Pd-L $_{\alpha}$ map (Fig. 3(c) and (d), respectively) shows that the large and medium scale features in each match up quite well. For instance, the location and size of the particles present in the nominal structure are faithfully reproduced in the HAADF output and the elemental map, with the signal-to-noise ratio SNR of the former being far superior to the latter due to the relative collection efficiencies of the two techniques. However, closer inspection of the data shows that a number of scan artifacts are present in the live output HAADF image. These include specimen alteration, as evidenced by the drop in HAADF intensity below the upper-left particle in Fig. 3(c), and mis-registration of the data due to either specimen charging or improper drift correction. The live-output HAADF signal indicates the true positioning of the electron probe with respect to the sample during the spectrum acquisition. Therefore, any defects present in the resulting image indicate that the XEDS signal collected from that particular pixel does not accurately represent the chemistry expected at that particular specimen position. Since the noise level present in the elemental maps is far higher than in the HAADF image, some of these problems are not readily apparent until the live-output HAADF signal is inspected. In the end, while the overall quality of the dataset is sufficient to

confirm the presence of Pd in the intense particle regions of the HAADF image, this experiment clearly shows the deficiencies inherent in the single-scan SI acquisition method to robustly map at high spatial resolution.

ESSI analysis of the same catalyst was carried out over a larger specimen area, but with a higher density of pixels (256×256), thus preserving the pixel size of the data set compared to the single-scan measurement. In this case, the analysis is carried out over the full region of interest rather than a pre-defined sub-region, and drift is corrected using data from the analytical area rather than a remote area (as in the single-scan acquisition). The total dwell time per pixel was the same as that used in the single-scan SI acquisition (60 ms). However, in this case, the total analysis time was reached by collecting 6000 frames using a per-pixel dwell time of 10 μ s. The resulting STEM-HAADF image shown in Fig. 4(a) represents the sum of all 6000 images acquired during this measurement, while the image in Fig. 4(b) shows the HAADF output of the first frame. As was the case for single-scan SI, comparing the elemental maps and the HAADF signal in the initial image shows that the structure of the carbon support and the overall distribution of the Pd particles agree quite well with each other. However, in this case, the HAADF output and the elemental maps are free from artifacts such as those seen previously in the single-scan images (Figs. 3(c) and 4(d)), and thus more accurately represent the true underlying composition. Finally, an ancillary benefit that results from the ability to analyze larger areas at similar spatial resolutions is demonstrated by the color overlay in Fig. 4(e). Whereas only Pd particles and the

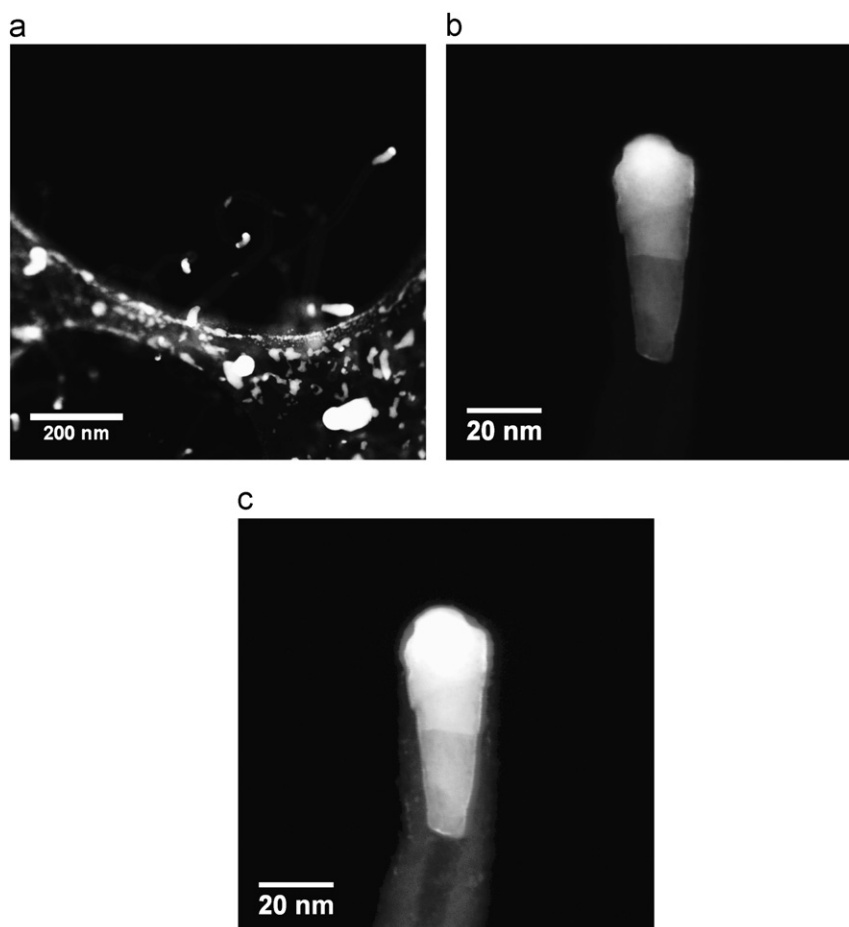


Fig. 5. STEM-HAADF images acquired from a specimen consisting of CNTs grown on Au–Ni catalyst particles. (a) Low-magnification image showing the distribution of nanotubes with respect to the metal particles, (b) higher magnification image showing the heterogeneous distribution of the two metal constituents present within an individual particle, and (c) another view of the image in (b) with the intensity levels saturated in order to reveal the position of the nanotube with respect to the particle.

C support were detected in the SI acquired using the slow-scan approach, the data acquired from a larger area via ESSI also isolated a third constituent (shown in green) that consisted of silicon oxide and titanium oxide impurity particles located on or within the carbon support.

3.3. Probing the chemistry of individual nanoparticles at high spatial resolution

The ESSI approach was also applied to individual bimetallic nanoparticles at high spatial resolution in an attempt to understand the spatial distribution of the two constituents. Au–Ni particles were used as catalysts for CNT growth carried out in an environmental TEM [15], which resulted in a dense forest of 1-D carbon nanostructures shown in Fig. 5(a). In-situ TEM imaging of the particles revealed that, while they exhibited a spherical morphology after heating to the reaction temperature, significant changes in their shape occurred after introduction of the acetylene gas and the resulting CNT growth. Most notably, the particles become elongated, consisting of a conical tip situated inside the CNT and a spherical capping region located outside the CNT growth region. In addition, sudden changes in the HR-TEM image contrast were observed from various areas within each particle during growth, suggesting that either a structural change or a chemical phase separation had occurred. In order to probe these changes, the particles were examined ex-situ using the aberration-corrected AEM. Examination of the individual particles

via STEM-HAADF imaging at higher-magnification revealed that the particles had retained their elongated structure after cooling to room-temperature. In addition, the atomic-number dependence of the HAADF image intensity suggests that a complex, heterogeneous distribution of the constituent metals exists within each particle (Fig. 5(b)), with three distinct regions being identified: (1) a pseudo-hemispherical Au-rich cap, (2) an elongated Ni-rich core, and (3) a Au-enriched skin layer surrounding the core. Saturation of the image contrast (Fig. 5(c)) demonstrates that the cap region exists outside the CNT, suggesting that it plays at most a secondary role in catalyzing the reaction while the active portion of the particle is located within the CNT.

In order to more quantitatively describe the elemental composition of these particles, XEDS spectrum imaging was employed in both single-scan and ESSI modes. The particles analyzed in this case were typically suspended over a hole in the SiO_x support film, and were anchored in place only by the attached CNT. As such, many of the single-scan acquisitions failed when the particle being analyzed suddenly disappeared due to scission of the CNT after prolonged exposure to the electron probe. A successful result of the single-scan SI analysis is presented in Fig. 6. Comparing the color-overlay (Fig. 6(b)) of the individual elemental maps (Ni-K α , Au-M α +Au-L α , and C-K α) with the STEM-HAADF image acquired prior to analysis (Fig. 6(a)) suggests that the structure revealed by the XEDS data faithfully captures that of the particle. Three distinct regions are identified in this image: (1) a Au-rich cap, (2) a Ni-rich core, and (3) the CNT itself.

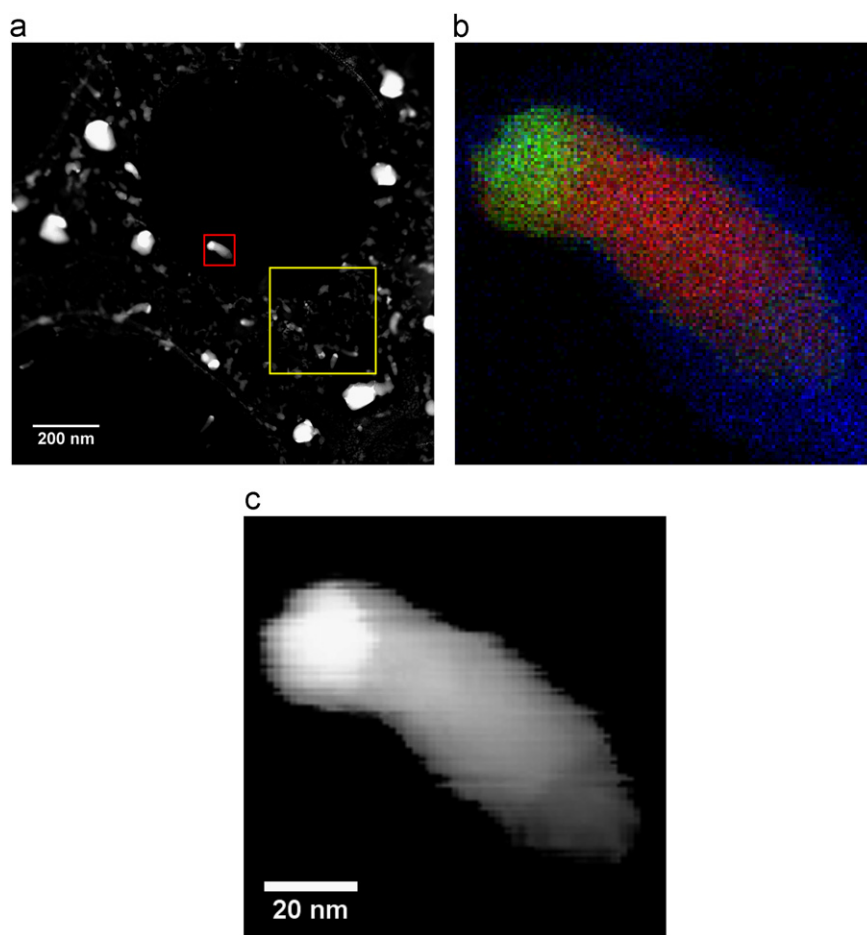


Fig. 6. Results of a single-scan XEDS spectrum image acquisition from a bimetallic Au–Ni catalyst particle used for CNT growth. (a) STEM-HAADF image and experimental setup showing the acquisition area and drift-correction reference area (red and yellow boxes, respectively). (b) Color-overlay showing the spatial extent of the Au (M α +L α) (green), Ni-K α (red), and C-K α (blue) signals. (c) Real-time HAADF detector output acquired during SI acquisition. Scale bar in (b) is the same as in (c). (For interpretation of the references to color in this figure legend, the reader is referred to the web version of this article.)

However, data related to the skin-layer were not isolated, and the reason for this is indicated by the real-time HAADF output (Fig. 6(c)), which shows a mis-registration of the data occurring on the level of a few scan pixels. If the XEDS maps had been analyzed without consulting the live-output HAADF image, this mis-registration would have gone unnoticed and resulted in erroneous analysis.

In contrast, similar data acquired using the ESSI method are presented in Fig. 7. In this case, even though the particle was suspended over a hole in the SiO_x film, the fast scan rate, coupled with real-time drift correction, allows for a more reliable characterization of the subtle features within these particles. The integrated HAADF output matches quite well with the HAADF output acquired prior to analysis (Fig. 7(a) and (b), respectively). The corresponding elemental maps are shown in Fig. 7(c)–(e), and a color overlay of the Au and Ni maps is shown in Fig. 7(d). Clearly, the quality of the given maps has improved significantly from those of maps collected using the single-scan SI method. In particular, the Au-rich skin layer has now been resolved, whereas the mis-registration occurring in the previous dataset prevented its analysis. The improved stability of the particle under the fast-moving electron probe relative to that observed during the single-scan acquisition is likely related to energy-dissipation mechanisms. In ESSI, the time spent at any given point on the specimen is spread over the course of the entire acquisition, and this allows for any deposited charge or energy transferred at this point in the specimen to be transported away while the probe is scanned over the rest of the analytical area. In the single-scan

approach, the total dose being delivered to each point on the specimen is delivered at once, and thus such relaxation mechanisms are severely limited.

As reported in our previous paper [15], the ESSI data, once properly segmented, indicate that only a small fraction of the nominal Au loading actually takes part in the reaction process, while the remainder (i.e. the capping structure) plays a secondary role that is not yet understood. This application clearly demonstrates the benefits of utilizing the ESSI method for nanoparticle characterization at high spatial resolutions.

3.4. Future applications of ESSI

Recently, the introduction of silicon drift detectors (SDD) into TEM/STEM columns has increased the collection solid-angle nearly five-fold over the typical side-entry Si(Li) detector. Systems based on this technology are now available, and results showing atomic-resolution XEDS with high SNR have been reported [17]. The substantial leap in the X-ray collection efficiency for XEDS in the AEM makes it comparable to EELS in terms of the detection limits of the two techniques, and, since windowless SDD detectors are now available, the sensitivities to low-Z elements exhibited by EELS and XEDS also approach similar values [18].

While the addition of an SDD detector to an AEM column allows for high-speed mapping of nano- and atomic-scale structures, truly quantitative analysis still requires the collection of as many X-rays as possible in the course of a spectrum image

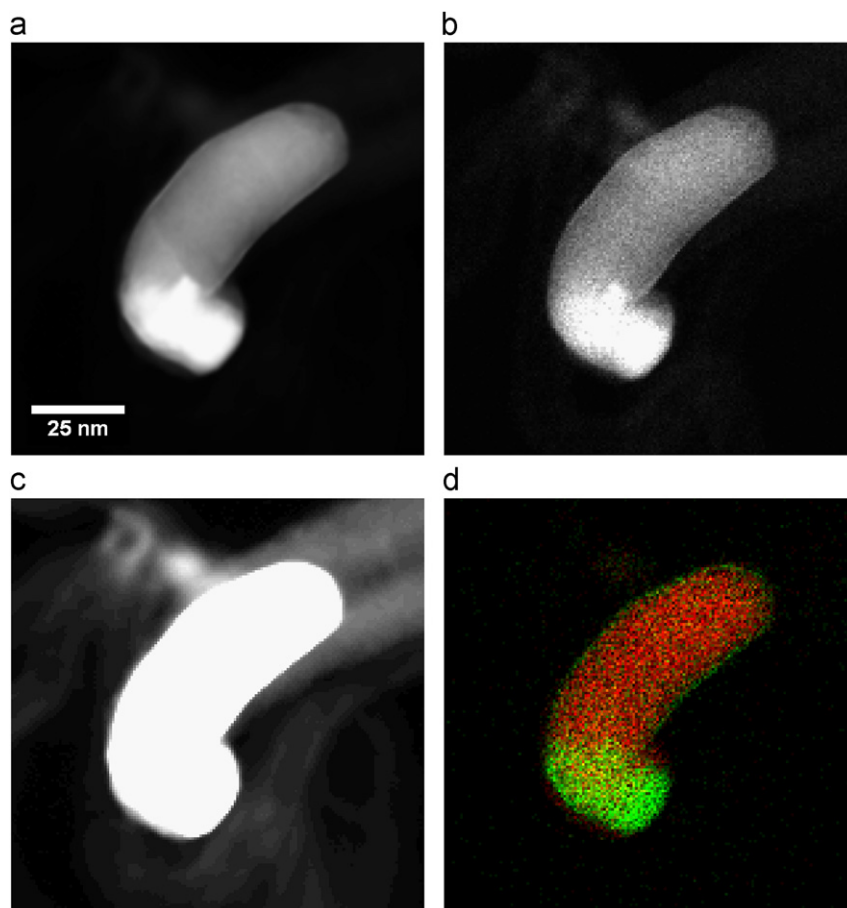


Fig. 7. Results of ESSI acquisition from an individual Au–Ni catalyst particle used for CNT growth. (a) STEM-HAADF integrated over the entire acquisition, (b) initial STEM-HAADF image acquired at the outset of acquisition, (c) same image as in (b) with gray levels saturated to reveal the extent of the CNT, and (d) color overlay showing the distributions of the Au-($M\alpha+L\alpha$) (green) and Ni- $K\alpha$ (red) signals. Scale bars in all images are the same as that in (a). (For interpretation of the references to color in this figure legend, the reader is referred to the web version of this article.)

acquisition. To combine the power of atomic-resolution XEDS with the quantitative algorithms already developed, demands a truly robust approach to data acquisition. Employing the ESSI approach to spectrum imaging in this context may offer a way to bridge this gap.

4. Conclusions

ESSI has been carried out in an aberration-corrected AEM for the characterization of nanoscale structures at high spatial resolution, and the technique was compared to conventional single-scan spectrum imaging. The limited instantaneous dwell time per pixel in combination with the real-time drift-correction enabled by ESSI makes possible a robust localization of the XEDS signal generated within the AEM such that it can be more confidently assigned to a given point on the specimen. Combining the ESSI technique with recent developments in detector hardware could potentially offer a powerful technique for quantitative, atomic-scale elemental spectroscopy.

Acknowledgments

Some of this work was carried out with the assistance of the NRC postdoctoral research associateship program. In addition, the authors would like to thank a number of people for sample preparation and discussions. The catalyst sample was provided by Dr. Jennifer Edwards (Cardiff University, UK). The misfit-layer compound was prepared by Dr. Michael Anderson (Global Foundries, Inc., USA; formerly NIST). Preparation and environmental-TEM characterization of the Au–Ni catalyzed CNT specimen were performed by Dr. Renu Sharma (NIST, USA). Finally, the authors

would like to acknowledge the assistance of Scott Davilla (4Pi, Inc., USA) for assistance in data processing.

References

- [1] S.J. Pennycook, P.D. Nellist (Eds.), *Scanning Transmission Electron Microscopy*, Springer, New York, NY, 2011.
- [2] M. Varela, S. Findlay, A.R. Lupini, H. Christen, *Physical Review Letters* 92 (2004) 3–6.
- [3] D.A. Muller, L.F. Kourkoutis, M. Murfitt, J.H. Song, H.Y. Hwang, J. Silcox, N. Dellby, O.L. Krivanek, *Science* 319 (2008) 1073–1076.
- [4] S.J. Pennycook, M. Varela, A.R. Lupini, M.P. Oxley, M.F. Chisholm, *Journal of Electron Microscopy* 58 (2009) 87–97.
- [5] A.J. D'Alfonso, B. Freitag, D. Klenov, L.J. Allen, *Physical Review B* 81 (2010) 2–5.
- [6] M. Watanabe, M. Kanno, E. Okunishi, *JEOL News* 45 (2010) 8–15.
- [7] M. Watanabe, C.J. Kiely, D. Ackland, A. Burrows, *Microscopy and Microanalysis* 12 (2006) 515–526.
- [8] M. Watanabe, in: S.J. Pennycook, P.D. Nellist (Eds.), *Scanning Transmission Electron Microscopy: Imaging and Analysis*, 1st ed., Springer, New York, NY, 2011, pp. 291–351.
- [9] D.B. Williams, C.B. Carter, *Transmission Electron Microscopy: A Textbook for Materials Science*, second ed., Springer, New York, 2009.
- [10] J.I. Goldstein, D.E. Newbury, D.C. Joy, C. Lyman, P. Echlin, E. Lifshin, L. Sawyer, J.R. Michael, *Scanning Electron Microscopy and X-Ray Microanalysis*, third ed., Springer, New York, NY, 2003. (pp. 182–184).
- [11] R.B. Mott, J.J. Friel, *Journal of Microscopy* 193 (1999) 2–14.
- [12] S. Davilla, *Microscopy and Microanalysis* 13 (2007) 1344–1345.
- [13] C.L. Heideman, R. Rostek, M.D. Anderson, A.A. Herzing, I.M. Anderson, D.C. Johnson, *Journal of Electronic Materials* 39 (2010) 1476–1481.
- [14] S. Walck, J. McCaffrey, *Thin Solid Films* 308 (1997) 399–405.
- [15] R. Sharma, S.-W. Chee, A.A. Herzing, R. Miranda, P. Rez, *Nano Letters* 11 (2011) 2464–2471.
- [16] J. Goldstein, D.B. Williams, G. Cliff, in: D.C. Joy, A.D. Romig, J.I. Goldstein (Eds.), *Principles of Analytical Electron Microscopy*, second ed., Plenum Publishing Corp., New York, 1986, pp. 155–217.
- [17] D. Klenov, B. Freitag, H. von Harrach, A. D'Alfonso, L. Allen, *Microscopy and Microanalysis* 17 (2011) 598–599.
- [18] H.S. von Harrach, D. Klenov, B. Freitag, P. Schlossmacher, P.C. Collins, H.L. Fraser, *Microscopy and Microanalysis* 16 (2010) 1312–1313.